This is a repository copy of *Parameterisation and Online States Estimation of High-Energy Lithium-Titanate Cells*.

White Rose Research Online URL for this paper:
https://eprints.whiterose.ac.uk/135065/

Version: Accepted Version

Parameterisation and Online States Estimation of High-Energy Lithium-Titanate Cells

S. Nejad, D. T. Gladwin, M. P. Foster, and D. A. Stone

Department of Electronic and Electrical Engineering
University of Sheffield
Sheffield, United Kingdom
Shahab.Nejad@Sheffield.ac.uk

Abstract—**In 2013, the University of Sheffield commissioned a 1 MWh lithium-titanate (LTO) battery energy storage system (BESS), directly connected to the grid through an 11 kV feed. With a view to later on develop a comprehensive model structure for the whole battery pack – key to many online battery management system (BMS) operations – in this paper, an in-depth frequency-domain analysis is performed on one of the constituent 2.3 V 20 Ah LTO cells, using a potentiostatic sine-swept method. A first-order resistor-capacitor (RC) equivalent-circuit model is put forward, capable of representing the LTO cell's impedance magnitude with an error of less than 0.1 mΩ. Thereafter, the performance of the proposed one-RC model structure for online SOC estimation is experimentally verified using the Extended Kalman Filter (EKF). The verification test is performed on a dynamic pulsed-power profile, derived from a real grid frequency-support service that is offered by several BESSs in the UK.**

Keywords—Lithium-Titanate; Battery; Equivalent-Circuit Modelling; Online; Kalman Filter; State-of-Charge; Estimation

I. INTRODUCTION

The ever-increasing penetration of renewable energy sources (e.g. wind, solar, tidal) and the trending uptake of smart-grid technologies by distribution network operators (DNOs), such as distributed generation (DG) systems [1], has created instability issues in grid voltage and frequency profiles, often caused by poor reactive power management and lack of load-frequency control in DG systems [1]. As a remedy, large-scale battery energy storage systems (BESSs), ranging from several megawatts [2] to a few tens of megawatts [3], have recently emerged to provide a variety of ancillary services [4] to supplement the grid's power quality around the work.

Recent advances in battery chemistry technologies, (e.g. lithium-iron, lithium-nickel, lithium-titanate) have allowed for significant improvements in large-scale battery energy storages in terms of higher volumetric energy capacities, better round-trip efficiencies, faster response times and lower maintenance requirements [5]. However, these advances, solely, play an inadequate role in satisfying the complex requirements of power and energy flow management in distribution networks. Hence, advances in battery management systems (BMSs) are also vital for ensuring an optimum and reliable battery operation, without risking the safety or longevity of the incorporated cells.

Integral to any modern BMS architecture is a set of intelligent algorithms (e.g. [6]) that provide estimates of various battery states and parameters, such as, battery internal

Fig. 1. Photograph of (left) 1 MWh Toshiba SCiB BESS consisting of 21,120 LTO cells, and (right) single 2.3 V 20 Ah test cell

resistance, state-of-charge (SOC – quantity of available charge compared to an initial capacity), state-of-power (SOP – quantity of available instantaneous sink/source power), and state-of-health (SOH – a measure of degradation in either energy capacity or power capability of a battery), which would otherwise be impractical to measure directly. These estimators often employ lumped-parameter equivalent-circuit models [7] to produce an adequate representation of the underlying transient reactions that govern the power response of the BESS.

In 2013, the University of Sheffield commissioned the first grid-tie lithium-titanate (LTO) BESS in the UK, called Willenhall Energy Storage System (WESS) [2], which consists of 21,120 20-Ah Toshiba LTO cells (Fig. 1) with a combined power/energy capacity of 2MW/1MWh. Now, due to the sheer number of cells involved and the complex BMS requirements for BESS energy/power control and management, it is crucial to have a firm understanding of the behavioural characteristics intrinsic to the utilised cell chemistry. Therefore, with a view to subsequently developing a comprehensive model for the 2MW/1MWh battery storage deployed at WESS [2], this paper reports on the frequency-domain analysis and equivalent-circuit modelling of one of the high-energy 20 Ah LTO cells (Fig. 1) used in the pack. The LTO cell is set to undergo a series of characterisation tests under laboratory conditions.

The tests include a static capacity measurement, an open-circuit voltage (OCV) extraction test to derive an OCV-SOC function that is required for online SOC estimation; and an electrochemical impedance spectroscopy (EIS) test to provide an analysis of the LTO cell's frequency response over its

operational SOC range and aid with the development of an electrical equivalent-circuit model structure, suitable for representing the LTO cell's transients. Finally, the performance of the LTO cell model for online SOC estimation is evaluated on a dynamic pulsed-power test profile that is derived based on a real grid-support frequency response application. The Extended Kalman Filter (EKF) – a nonlinear variation of the original Kalman Filter algorithm – is utilised to realise an online SOC estimation, which will be experimentally verified.

II. LTO CELL MODELLING

EIS is a well-known technique that is often employed to help with the understanding of various charge-transfer and capacitive reactions inherent to all cell chemistries. The general principle is to inject the cell with either a current (glavanostatic) or voltage (potentiostatic) sinusoid and measure its response, from which the cell's impedance can be calculated as a function of angular frequency ($\omega = 2\pi f$). In this work, a potentiostatic EIS regime, similar to that reported in [8], was applied to the LTO test cell over a frequency range of 5 mHz $\leq f \leq$ 5 kHz. The test was carried out over the cell's entire SOC range, at 10% granularity.

A. Cell Impedance Spectroscopy

For a potentiostatic EIS test, the cell's impedance, as a function of frequency, can be expressed as,

$$Z(\omega) = \frac{U}{I(\omega)} \angle \phi(\omega) \tag{1}$$

$$Z(\omega) = Z' + jZ'' \tag{2}$$

$$Z' = |Z| \cdot \cos(\phi), \qquad Z'' = |Z| \cdot \sin(\phi)$$

where U is the amplitude of the injected voltage signal, $I(\omega)$ is the measured current response, $\phi(\omega)$ is the phase angle and $Z(\omega)$ is the cell's impedance. In battery electroanalysis, it is common to display complex impedance data with Nyquist plots, where the negative imaginary (Z'') component of impedance is plotted against its real (Z') component.

Fig. 2 compares the Nyquist plots obtained for the 20 Ah LTO test cell with that of a 3.3 Ah lithium-iron (LFP) cell and a 3.6 Ah lithium-nickel (NMC) cell, all characterised 25°C and 50% SOC. It is evident that, compared to the LFP and NMC cell chemistries, the LTO cell has the lowest internal series resistance (i.e. point α where $Z'' = 0\ \Omega$). This is due to its metallic (titanate) coating of the anode electrode, which leads to a better ionic current conductivity, and thus, lower resistive losses at high current rates. This virtue makes LTO cells ideal for large-scale energy storage applications, where thermal management of the heat generated by the cells through internal resistive losses can curtail the performance of the whole pack.

Moreover, it can be seen from Fig. 2 that the LTO cell does not exhibit the typical depressed semicircles associated with the formation of solid electrolyte interface (SEI) film over the surface of the anode electrode and the charge-transfer resistance and double-layer capacitance at both electrodes [9]. Instead, the spectrum crosses the real axis (i.e. point α) at 5 Hz, with diffusional impedance dominating the spectrum from 5 Hz down to 5 mHz. This is represented by a 45° tail that runs upwards of
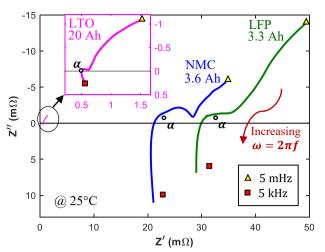

Fig. 2. Comparison of impedance spectra for LTO, NMC, and LFP cells, measured at 25°C and 50% SOC, over 5 mHz and 5 kHz
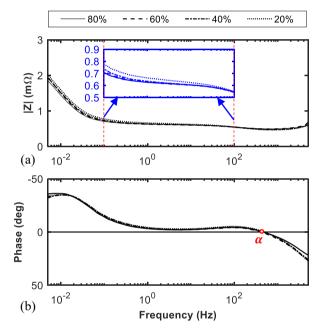

Fig. 3. Bode plots showing (a) magnitude and (b) phase of the LTO test cell's impedance obtained at 25°C, over several SOC levels

point α (i.e. 5 Hz) into the negative imaginary plane (i.e. approaching 5 mHz). Beyond 5 Hz, a large inductive loop is observable, which is inherent to LTO cell technology.

Fig. 3 presents the bode magnitude and phase plots for the LTO test cell, obtained at 25°C and SOC levels of 20%, 40%, 60% and 80%. Note that between 100 mHz and 100 Hz (blue subplot), the LTO cell has a fairly constant impedance response, behaving almost as an ideal resistor. This phenomenon can also be attributed to the metallic coating of the cell's anode, which implies that, instead of performing a frequency sweep (e.g. EIS method) to characterise the internal resistance of an LTO cell, it is possible to apply the cell with a single-frequency stimulant current in order to represent the cell's response over the frequency range of 100 mHz and 100 Hz.

B. Cell Model Structure

In online battery modelling and state estimation problems, it is common to employ electrical equivalent-circuit models to represent the battery's dynamics in real time. These models (e.g. Fig. 4) are usually comprised of a voltage source that describes the battery's OCV-SOC relationship, which is useful for online SOC estimation, and a resistor connected in series with a number of parallel RC branches. In [7], the authors have shown that a second-order RC model can sufficiently describe the short and long time-constant dynamics in LFP and NMC cells. However, as can be seen in Fig. 5, due to the dominant diffusional impedance effects in the tested LTO cell, a first-order RC model structure can be safely adopted to accurately mimic the cell's response under real-time conditions, while reducing unnecessary modelling complexity.
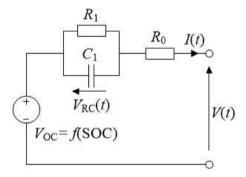

Fig. 4. One-*RC* battery model

Fig. 4 depicts a first-order RC equivalent-circuit battery model, named One-RC model hereafter, which consists of an OCV-SOC function $V_{OC}(SOC)$ to be defined later for the LTO cell in hand, R_0 that describes the series-resistance of the cell and $R_1 \| C_1$ branch which aims to capture the diffusional effects within the cell over the tested frequency band. Considering the model structure proposed in Fig. 4, the LTO cell's voltage, $V(t)$, in the time domain, can be defined using a set of linear time-varying (LTV) equations,

$$\left. \begin{aligned} \dot{V}_{RC} &= -\frac{V_{RC}(t)}{\tau_1} + \frac{I(t)}{C_1} \\ V(t) &= V_{OC}(SOC) - V_{RC}(t) - I(t) \cdot R_0 \end{aligned} \right\} \quad (3)$$

where $V_{RC}(t)$ is the transient voltage drop across $R_1 \| C_1$, $\tau_1 = R_1 C_1$ is the time constant associated with the diffusional effects and $I(t)$ is the throughput current.

C. Offline Model Parameterisation

In order to investigate the SOC-dependency of the LTO cell model parameters and set the initial conditions for the dual-EKF estimator, the nonlinear Levenberg-Marquardt algorithm [10] was used to fit the One-RC model to the EIS-obtained data over the cell's entire SOC range of 0%-100%. Subsequently, the model parameters R_0, R_1 and C_1 were identified.

Fig. 5 demonstrates the frequency-domain performance of the One-RC model with the parameters identified at 25°C and 50% SOC. The curve-fitting was performed over the negative imaginary plane, where meaningful insights regarding the internal series-resistance and diffusional properties of the cell
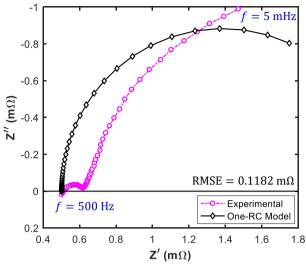

Fig. 5. Impedance spectrum for 20 Ah LTO cell, showing EIS-obtained data and One-*RC* model fit for 5 mHz ≤ f ≤ 500 Hz

can be provided, neglecting the cell's inductive reactance at frequencies above 5 Hz. Evidently, the chosen RC model order of one is capable of accurately simulating the frequency response of the LTO test cell, with a root-mean-square error (RMSE) term of only 0.1182 mΩ. The RMSE term was calculated using (4), where $\omega_1 = 2 \times \pi \times 5$ rad/s and $\omega_0 = 2 \times \pi \times 0.005$ rad/s. The fitting performance of the One-RC model for other SOC values can be found in Table I.

$$\text{RMSE} = \sqrt{\frac{1}{\omega_1 - \omega_0} \int_{\omega_0}^{\omega_1} \left(|Z_{EIS}(\omega)| - |Z_{mdl}(\omega)| \right)^2 \cdot df} \quad (4)$$

TABLE I
FITTING PERFORMANCE OF ONE-*RC* MODEL STRUCTURE AT SEVERAL SOCs

SOC (%)	RMSE (mΩ)
0	0.37128
10	0.18817
20	0.15303
30	0.13085
40	0.10451
50	0.11823
60	0.14065
70	0.11936
80	0.1248
90	0.1426
100	0.1584

Fig. 6 presents the identified One-RC model parameters for the 20 Ah LTO test cell as a function of SOC; an inverse correlation between the cell's series-resistance (R_0) and its SOC can be seen, except at 100% SOC, where R_0 increases slightly. This phenomenon can be attributed to the poor charge acceptance of the cell when fully charged. In contrary to R_0, the variations in R_1 and C_1 with respect to SOC are more inconsistent, merely due to the fact that these two parameters aim to capture those intrinsically nonlinear diffusional reactions.
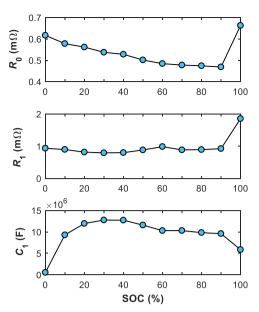
Fig. 6. Identified One-*RC* model parameters for LTO test cell at 25°C

Fig. 7. OCV-SOC relationship for the LTO test cell at 25°C

TABLE II
OCV MODEL COEFFICIENTS IDENTIFIED AT 25°C

Coefficient	Value
p_8	78.517
p_7	-357.28
p_6	659.75
p_5	-630.79
p_4	330.24
p_3	-91.478
p_2	11.667
p_1	-0.05529
p_0	2.0751

III. ONLINE BATTERY IDENTIFICATION AND SOC ESTIMATION

Assuming a small sampling period Δt and discretised time step k, battery SOC can be defined in its discrete form as,

$$\text{SOC}_k = \text{SOC}_{k-1} - \left(\frac{\eta \cdot \Delta t}{Q_{\max}}\right) \cdot I_k \qquad (5)$$

where $Q_{\max} = 3600\text{s} \times 20.14\text{Ah}$ is the LTO cell's columbic capacity, η is the columbic efficiency (assumed unity), and I_k is instantaneous current amplitude at discrete time-step k. In this paper, a recursive dual-EKF estimator [11] is designed to estimate SOC. To this end, an accurate relationship between the battery's OCV and its SOC needs to be established.

A. OCV Modelling

In order to describe the LTO cell's OCV curve as a function of SOC, a pulsed-current test, similar to that reported in [11], has been applied herein. Fig. 7 presents the resulting OCV-SOC relationship for the LTO cell at 25°C, measured after 30 minutes of voltage recovery at every $\Delta\text{SOC} = 10\%$ step. In contrast to the flat OCV curves inherent to LFP cells [11], the LTO cell has a fairly steep and monotonic OCV-SOC relationship that will result in reduced modelling uncertainties, when using any online OCV-based SOC estimator (e.g. EKF).

Another interesting fact about the observed OCV curve in Fig. 7 is that a dominant phase-transformation stage seems to occur between 50% and 70% SOC. To capture this phenomenon and be able to accurately model the OCV-SOC curve shown in Fig. 7 for online SOC estimation, in this paper, an eighth-order polynomial function is derived.

$$V_{\text{OC}}(\text{SOC}) = p_8 \times \text{SOC}^8 + \cdots + p_1 \times \text{SOC} + p_0 \qquad (6)$$

where coefficients $p_{0\to8}$ are realised through curve-fitting the polynomial given above to the experimentally-measured OCV data for both charge and discharge curves at 25°C. These coefficients are summarised in Table II.
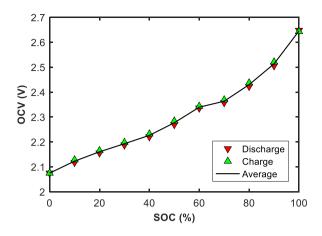
B. State-Space Equations

In order to use the dual-EKF algorithm for online battery identification and SOC estimation, the LTV equations given by (3) must be transformed into a discrete-time state-space form.

$$\mathbf{x}_k = \mathbf{A}_k\mathbf{x}_{k-1} + \mathbf{B}_k\mathbf{u}_k + \mathbf{w}_k; \; \boldsymbol{\theta}_k = \boldsymbol{\theta}_{k-1} + \mathbf{e}_k;$$
$$\mathbf{y}_k = \mathbf{C}_k\mathbf{x}_k + \mathbf{D}_k\mathbf{u}_k + \mathbf{v}_k \qquad (7)$$

where, assuming a sampling period of Δt, the state matrix $\mathbf{x}$, observation matrix $\boldsymbol{y}$ and input matrix $\mathbf{u}$ can be defined by (8), and the time-varying matrices $\mathbf{A}_k$, $\mathbf{B}_k$, $\mathbf{C}_k$ and $\mathbf{D}_k$ by (9). $\mathbf{w}_k \sim N(0, \mathbf{Q}_k)$ is the process noise, $\mathbf{e}_k \sim N(0, \boldsymbol{\Sigma}_k)$ is a small white noise that evolves the parameter matrix $\boldsymbol{\theta}$, and $\mathbf{v}_k \sim N(0, \mathbf{R}_k)$ is the observation noise.

$$\mathbf{x}_k = [\text{SOC}_k \quad V_{\text{RC},k}]^\text{T}; \; \boldsymbol{\theta}_k = [R_{0,k} \quad R_{1,k} \quad \tau_{1,k}]^\text{T};$$
$$\boldsymbol{y}_k = V_k; \; \mathbf{u}_k = I_k \qquad (8)$$

$$\mathbf{A}_k = \begin{bmatrix} 1 & 0 \\ 0 & e^{-\frac{\Delta t}{\tau_1}} \end{bmatrix}; \; \mathbf{B}_k = \begin{bmatrix} -\dfrac{\Delta t}{Q_{\max}} \\ R_{1,k}\left(1 - e^{-\frac{\Delta t}{\tau_{1,k}}}\right) \end{bmatrix};$$

$$\mathbf{C}_k^\text{x} = \begin{bmatrix} \dfrac{\partial V_{\text{OC}}(\text{SOC}_k)}{\partial \text{SOC}_k} & -1 \end{bmatrix}; \; \mathbf{D}_k = [-R_{0,k}]. \qquad (9)$$

In order to compute the Kalman gain, $\mathbf{C}_k^\theta$, for the weight filter, total-differential expansion of the output function, V_k, is required with respect to $\boldsymbol{\theta}$, which can be given recursively as,

1. **Initialisation:**

$\hat{\mathbf{x}}_0^+ = [SOC_0, 0]^T$, $\qquad \hat{\boldsymbol{\theta}}_0^+ = [0.0128, 0.0023, 35.54]^T$

$\mathbf{Q}_0^x = \text{diag}_n\{1 \times 10^{-10}\}$, $\qquad \mathbf{P}_{\hat{x},0}^+ = \text{diag}_n\{10\}$, $\qquad \mathbf{R}_0^x = \text{diag}_m\{10\}$

$\mathbf{Q}_0^\theta = \text{diag}_q\{1 \times 10^{-12}\}$, $\qquad \mathbf{P}_{\hat{\theta},0}^+ = \text{diag}_q\{10\}$, $\qquad \mathbf{R}_0^\theta = \text{diag}_m\{100\}$

2. **Time-update equations:**

$\hat{\mathbf{x}}_k^- = \mathbf{A}_{k-1}\hat{\mathbf{x}}_{k-1}^+ + \mathbf{B}_{k-1}\mathbf{u}_{k-1}$, $\qquad \hat{\boldsymbol{\theta}}_k^- = \hat{\boldsymbol{\theta}}_{k-1}^+$

$\mathbf{P}_{\hat{x},k}^- = \mathbf{A}_{k-1}\mathbf{P}_{\hat{x},k-1}^+\mathbf{A}_{k-1}^T + \mathbf{Q}^x$, $\qquad \mathbf{P}_{\hat{\theta},k}^- = \mathbf{P}_{\hat{\theta},k-1}^+ + \mathbf{Q}_k^\theta$

3. **Measurement-update equations:**

$\mathbf{L}_k^x = \mathbf{P}_{\hat{x},k}^-(\mathbf{C}_k^x)^T[\mathbf{C}_k^x\mathbf{P}_{\hat{x},k}^-(\mathbf{C}_k^x)^T + \mathbf{R}_k^x]^{-1}$

$\hat{\mathbf{x}}_k^+ = \hat{\mathbf{x}}_k^- + \mathbf{L}_k^x[\mathbf{y}_k - \mathbf{C}_k^x\hat{\mathbf{x}}_k^- - \mathbf{D}_k\mathbf{u}_k]$

$\mathbf{P}_{\hat{x},k}^+ = (\mathbf{I} - \mathbf{L}_k^x\mathbf{C}_k^x)\mathbf{P}_{\hat{x},k}^-(\mathbf{I} - \mathbf{L}_k^x\mathbf{C}_k^x)^T + \mathbf{L}_k^x\mathbf{R}_k^x(\mathbf{L}_k^x)^T$

$\mathbf{L}_k^\theta = \mathbf{P}_{\hat{\theta},k}^-(\mathbf{C}_k^\theta)^T[\mathbf{C}_k^\theta\mathbf{P}_{\hat{\theta},k}^-(\mathbf{C}_k^\theta)^T + \mathbf{R}_k^\theta]^{-1}$

$\hat{\boldsymbol{\theta}}_k^+ = \hat{\boldsymbol{\theta}}_k^- + \mathbf{L}_k^\theta[\mathbf{y}_k - \mathbf{C}_k^\theta\hat{\mathbf{x}}_k^- - \mathbf{D}_k\mathbf{u}_k]$

$\mathbf{P}_{\hat{\theta},k}^+ = (\mathbf{I} - \mathbf{L}_k^\theta\mathbf{C}_k^\theta)\mathbf{P}_{\hat{\theta},k}^-(\mathbf{I} - \mathbf{L}_k^\theta\mathbf{C}_k^\theta)^T + \mathbf{L}_k^\theta\mathbf{R}_k^\theta(\mathbf{L}_k^\theta)^T$

$$\mathbf{C}_k^\theta = \frac{dV_k}{d\boldsymbol{\theta}}\bigg|_{\boldsymbol{\theta}_k = \hat{\boldsymbol{\theta}}_k^-} = \frac{\partial V_k}{\partial \hat{\boldsymbol{\theta}}_k^-} + \frac{\partial V_k}{\partial \hat{\mathbf{x}}_k^-} \cdot \frac{d\hat{\mathbf{x}}_k^-}{d\hat{\boldsymbol{\theta}}_k^-}$$

$$\frac{\partial V_k}{\partial \hat{\mathbf{x}}_k^-} = \left[\frac{\partial V_{OC}(SOC_k)}{\partial SOC_k} \quad -1\right]$$

$$\frac{\partial V_k}{\partial \hat{\boldsymbol{\theta}}_k^-} = [-I_{k-1} \quad 0 \quad 0]$$ (10)

$$\frac{d\hat{\mathbf{x}}_k^-}{d\hat{\boldsymbol{\theta}}_k^-} = \begin{bmatrix} 0 & 0 & 0 \\ 0 & a_{2,2} & a_{2,3} \end{bmatrix}$$

where $a_{2,2} = I_{k-1} \cdot (1 - \exp(\Delta t/\tau_1))$ and $a_{2,3} = (\Delta t/\tau_1^2) \cdot (V_{RC,k-1} - I_{k-1}R_1) \cdot \exp(-\Delta t/\tau_1)$. Consequently, the LTO cell model parameters and states (including SOC) are estimated, in real time, using the recursive steps outlined in Table III, where $\mathbf{P}_{\hat{x},k}^+$ and $\mathbf{P}_{\hat{\theta},k}^+$ are given in their Joseph forms [11].

IV. EXPERIMENTAL VERIFICATION

A. Dynamic Pulsed-Power Test Profile

To assess the performance of the One-RC model for online LTO cell identification and SOC estimation, a dynamic pulsed-power profile is devised based on a real-application UK grid frequency-support service, namely the Enhanced Frequency Response (EFR) service [12] that the 1 MWh LTO battery system at WESS provides. Fig. 8 presents a 24-hour cell power profile derived from a historical frequency dataset, namely that of 21st October 2015, which is scaled down for a cell according to the 2C rule, satisfying the requirements for a maximum power equal to twice the cell's Watt-hour capacity, i.e. $2 \times 2.3V \times 20Ah = 92$ W. However, for the dynamic test profile used here, the peak power that the LTO cell has to withstand during discharge is ~29 W and that during charge is ~30 W.
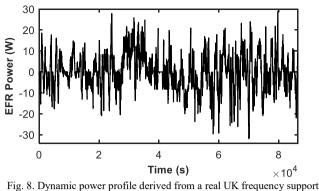

Fig. 8. Dynamic power profile derived from a real UK frequency support service delivered by grid-tie energy storage systems

During an EFR service, the battery must be able to respond to both high and low frequency events, by importing and exporting power, respectively; thus, a SOC band of 45-55% is often desired. In this instance, prior to applying the LTO cell with the dynamic EFR profile, the cell was fully charged and then discharged to 50% SOC. Finally, the dual-EKF algorithm is implemented using the initial conditions given in Table III.

The setup used to carry out the experimentations on the 2.3 V 20 Ah LTO test cell consisted of a multi-channel Maccor 4000-series battery tester with measurement accuracies of ±0.02% for the voltage and ±0.05% for the current. Each channel has a voltage and current range of 0-20 V and ±10 A, respectively. The profile shown in Fig. 8 requires a maximum power of ~30 W which can result in a maximum current of 20 A when the cell is at its lowest voltage of 1.5 V. Thus, two Maccor channels were connected in parallel to suffice this requirement.

B. Results and Discussion

Fig. 9 presents the terminal voltage and OCV estimation performance of the One-RC cell model, when applied with a dual-EKF estimator. It indicates that the estimated terminal voltage tracks the measured profile very well, with the terminal voltage errors, shown in Fig. 9(b), being generally below 5 mV or 0.2% of the measured values. This excellent performance is owed to the recursive computation of the Kalman gains for both states and weight filters in Table III, which adaptively minimises an error term between the observed and estimated quantities.

To verify the convergence and tracking capability of the online SOC estimator for the 20 Ah LTO cell in hand, three filter initialisation scenarios were tested; SOC_0 set to its true value of 50%, SOC_0 set to an erroneous value of 20%, and SOC_0 set to an erroneous value of 80%. Fig. 10 presents the results under the three initialisation conditions, together with a plot of the calculated errors with respect to a reference SOC (Ref. SOC in Fig. 10) that was obtained by relying on the accuracy of the battery tester's current sensors and using the coulomb-counting method. In all cases, an excellent agreement between the estimations and 'Ref. SOC' can be observed. This is attributed to the perfectly captured OCV-SOC relationship by (6) and the high fidelity of the One-RC model structure as proven in Table I. Furthermore, under both erroneous SOC initialisation scenarios, the EKF achieves convergence to within ±5% error bounds after only 100 seconds of operation. This further verifies the robustness the designed EKF SOC estimator.
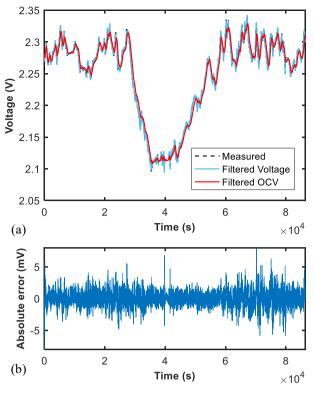
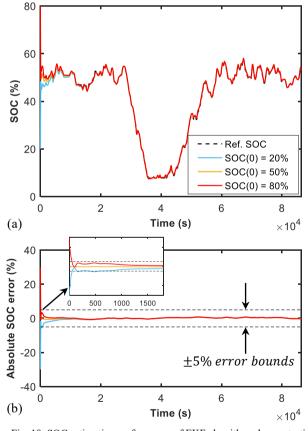Fig. 9. LTO cell terminal voltage and OCV estimation performance on a dynamic pulsed-power profile at 25°C

Fig. 10. SOC estimation performance of EKF algorithm, demonstrating convergence under various initialisation conditions

V. Conclusion

This paper reported on the modelling and identification of a high-energy LTO cell, with a view to later on develop a comprehensive battery model for a 1 MWh BESS installed in the UK, which is comprised of 21,120 of the tested cells. Following a frequency-domain analysis using the EIS method, the LTO cell was found to have a dominant diffusional behaviour. A first-order RC model structure with only one long time-constant transient was then put forward to effectively represent the cell's impedance response over its entire SOC range. Thereafter, a dual-EKF estimator was deigned to verify the performance of the proposed one-RC model structure for online cell SOC estimation. Experimental results have shown that the combination of the one-RC model and the dual-EKF estimator can lead to excellent voltage and SOC estimation performance in the tested 2.3 V 20 Ah LTO cell, with a SOC convergence time of only 100 seconds, when tested on a 24-hour dynamic pulsed-power profile.

References

[1] G. A. Quiroga, H. Kagan, J. C. C. Amasifen, C. F. M. Almeida, N. Kagan, and E. Vicentini, "Study of the DG impact on distributed networks, focused on quality of power," in Harmonics and Quality of Power (ICHQP), 2016 17th International Conference on, 2016, pp. 855–860.

[2] T. Feehally et al., "Battery energy storage systems for the electricity grid: UK research facilities," 2016.

[3] M. Świerczyński, R. Teodorescu, C. N. Rasmussen, P. Rodriguez, and H. Vikelgaard, "Overview of the energy storage systems for wind power integration enhancement," in Industrial Electronics (ISIE), 2010 IEEE International Symposium on, 2010, pp. 3749–3756.

[4] X. Tan, Q. Li, and H. Wang, "Advances and trends of energy storage technology in Microgrid," Int. J. Electr. Power Energy Syst., vol. 44, no. 1, pp. 179–191, 2013.

[5] H. Qian, J. Zhang, and W. Yu, "A High-Efficiency Grid-Tie BESS," IEEE Trans. Power Electron., vol. 26, no. 3, pp. 886–896, Mar. 2011.

[6] A. T. Elsayed, C. R. Lashway, and O. A. Mohammed, "Advanced Battery Management and Diagnostic System for Smart Grid Infrastructure," IEEE Trans. Smart Grid, vol. 7, no. 2, pp. 897–905, Mar. 2016.

[7] S. Nejad, D. T. Gladwin, and D. A. Stone, "A systematic review of lumped-parameter equivalent circuit models for real-time estimation of lithium-ion battery states," J. Power Sources, vol. 316, pp. 183–196, 2016.

[8] S. Nejad, D. T. Gladwin, and D. A. Stone, "Sensitivity of lumped parameter battery models to constituent parallel-RC element parameterisation error," in Industrial Electronics Society, IECON 2014 - 40th Annual Conference of the IEEE, 2014, pp. 5660–5665.

[9] P. Verma, P. Maire, and P. Novák, "A review of the features and analyses of the solid electrolyte interphase in Li-ion batteries," Electrochim. Acta, vol. 55, no. 22, pp. 6332–6341, Sep. 2010.

[10] D. W. Marquardt, "An Algorithm for Least-Squares Estimation of Nonlinear Parameters," J. Soc. Ind. Appl. Math., vol. 11, no. 2, pp. 431–441, 1963.

[11] S. Nejad, D. T. Gladwin, and D. A. Stone, "Enhanced state-of-charge estimation for lithium-ion iron phosphate cells with flat open-circuit voltage curves," in Industrial Electronics Society, IECON 2015 - 41st Annual Conference of the IEEE, 2015, pp. 3187–3192.

[12] NGET, "Enhanced Frequency Response, Invitation to tender for pre-qualified parties V2.2," 2016. [Online]. Available: http://www2.nationalgrid.com/Enhanced-Frequency-Response.aspx.